RSC Advances

PAPER

View Article Online
View Journal | View Issue

Bi_2O_3 and BiOCl electrospun nanosheets and morphology-dependent photocatalytic properties†

Cite this: *RSC Adv.*, 2014, **4**, 29957

Veluru Jagadeesh Babu,*[a] R. S. R. Bhavatharini[b] and Seeram Ramakrishna*[bc]

Received 24th April 2014
Accepted 12th June 2014

DOI: 10.1039/c4ra03754e

www.rsc.org/advances

BiOCl and Bi_2O_3 nanosheet like structures were produced by electrospinning. The morphological changes were observed by changing precursor ($BiOCl_3$ and $Bi(NO_3)_3 \cdot 5H_2O$) concentrations. These nanosheets were analyzed by XRD, which reveals that the crystal structures of BiOCl and Bi_2O_3 belonged to tetragonal and beta-phase systems respectively. Both nanostructures were employed for the photodegradation of Alizarin Red S (ARS) dye under UV light (<390 nm) irradiation. BiOCl nanosheet like structures exhibited superior photocatalytic activity (PCA) for the degradation of ARS dye and their half-life was estimated from the kinetic plots of PCA. A plausible reaction mechanism is proposed for the PCA and discussed in detail.

Introduction

In recent years, novel layered/sheet-like structures of bismuth oxyhalides BiOX (X = Cl, Br, and I) have drawn much attention due to their optical properties and promising industrial applications.[1] Bismuth oxychloride (BiOCl) and bismuth oxide (Bi_2O_3) have potential for degradation of organic dyes[2,3] and non-biodegradable synthetic dyes.[4,5] BiOCl exhibits the tetragonal space group P_4/nmm and consists of stacked sheets of Cl–Bi–O–Bi–Cl held together by the nonbonding interaction through the Cl atoms along the *c*-axis.[6] In each sheet, a bismuth center is surrounded by four oxygen (O_2) and four chlorine (Cl) atoms in an asymmetric decahedral geometry. These tetragonal crystal structures of BiOCl can be flattened into sheet-like structures with a high aspect ratio. BiOCl had been used in several applications[2,7,8] because the strong intralayer bonding and the weak interlayer interactions (van der Waals) between the sheets would be favourable for work on highly anisotropic structures, as well as for improved electrical, optical, and mechanical properties. Owing to the unique sheet-like structure and high photocorrosion stability in the presence of redox couples, BiOCl has recently been used for photocatalysis[9,10] and in photoelectrochemical (PEC) applications.[2,8,11] Zhang *et al.*[2] reported that BiOCl exhibited better photocatalytic activity (PCA) on the methyl orange (MO) dye degradation, than did TiO_2 (P25, Degussa). On the other hand, Bi_2O_3 was proved to be a significant photocatalyst for the degradation of rhodamine B (RB) and MO dye under UV and visible-light irradiation, respectively.[3,5,12] Lin *et al.*[13] reported that the PCA of Bi_3O_4Cl (synthesized from BiOCl and Bi_2O_3 *via* a solid state reaction) was more effective for the degradation of MO dye than that of anatase TiO_2 under UV light irradiation.

In addition, low-dimensional nanostructures[14–16] could enhance the PCA enormously and, therefore, the preparation of nanostructured BiOCl and Bi_2O_3 are considered promising for photocatalytic applications. The nanoparticular BiOCl and Bi_2O_3 can be an efficient photocatalyst in decomposing methyl orange under UV irradiation.[2,3] However, bismuth oxide nanoparticles have limitations; for example, suspended nanoparticulate catalysts are easily lost in the process of the PCA reaction and separation, and may pollute treated water. In contrast, nanofibers, which also have potential for PCA applications, have already proven favourable because of their recycling properties.[17] One-dimensional (1D) nanostructures such as nanowires (NW), nanosheets (NS), nanorods (NR), and nanotubes (NT) enhance PCA due to their high surface areas.[11,17,18] 1D nanostructures are employed in various applications such as solving environmental (photocatalysis and water treatment)[19,20] and energy (electronics and photonics) issues.[21–23] In this context, photocatalysis is a "green" technique, which offers promising ways to completely remove toxic pollutants from the environment through its efficiency and broad suitability.[24] 1D nanostructures produced by electrospinning is straightforward and simple.[25–27] Wang *et al.*[28] reported that electrospun nanofibers of Bi_2O_3 exhibited significant PCA for degradation of the organic pollutant rhodamine B (RB). Furthermore, the Bi_2O_3 nanofibers could be easily recycled without decrease of PCA.

Herein, we report for the first time nanosheet-like structures from that of BiOCl and Bi_2O_3 electrospun nanofibers. The

[a]*UNAM-National Nanotechnology Research Center, Bilkent University, Ankara-06800, Turkey. E-mail: babu@unam.bilkent.edu.tr; Fax: +90 312 266 4365; Tel: +90 312 290 3584*

[b]*NUS Centre for Nanofibers and Nanotechnology, Nanoscience and Nanotechnology Initiative, National University of Singapore, Singapore-117576, Singapore. E-mail: seeram@nus.edu.sg*

[c]*Department of Mechanical Engineering, National University of Singapore, Singapore-117576, Singapore. Tel: +65 6516 2216*

† Electronic supplementary information (ESI) available: Additional UV photocatalytic ARS dye degradation studies for the Bi_2O_3 and BiOCl, being provided. See DOI: 10.1039/c4ra03754e

formation of these nanostructures and their morphology was observed at different precursor ($BiOCl_3$ and $Bi(NO_3)_3 \cdot 5H_2O$) concentrations varying from 1 to 4 wt%. Microscopy, spectroscopy and XRD were used for the characterization of nanostructures. The resultant nanostructures were employed for the degradation of ARS dye under UV light (<390 nm) irradiation. The comparative PCA study of the electrospun nanostructures of how BiOCl and Bi_2O_3 induces complete degradation of the ARS dye was carried out. A plausible mechanism for the PCA of BiOCl is proposed and explained.

Experimental section

Materials

Bismuth(III) nitrate pentahydrate ($Bi(NO_3)_3 \cdot 5H_2O$); 98%, bismuth(III) chloride ($BiCl_3$; 98%), polyacrylonitrile (PAN, MW = 150 000 Da), and *N*,*N*-dimethylformamide (DMF; anhydrous 99.8%) were obtained from Sigma Aldrich Chemical Company, Inc., St. Louis, MO, U.S. All chemicals were used without further purification.

Preparation

Bi_2O_3 nanofiber preparation. Nearly 10% (wt) of PAN powder was initially dissolved in DMF and stirred for about 2 h. After a reasonably miscible solution was obtained, nearly 1% w/v of $Bi(NO_3)_3 \cdot 5H_2O$ was added to the above DMF solution, then stirred for about 2 h to create a homogeneous solution for the electrospinning. Similar solution preparations were repeated for the variable concentrations (2, 3, and 4 wt%) of $Bi(NO_3)_3 \cdot 5H_2O$. The procedure for the electrospinning was followed as published previously.[25] The above electrospinning solution was drawn up into a 10 mL syringe with 21 G 1/2 gauge needle. The fiber deposition parameters (flow rate, applied voltage, drum rotation speed, *etc.*) were optimized until uniform nanofibers without bead formation was obtained. The flow rate was maintained at 0.5 mL h^{-1} (for Bi_2O_3) and 1.0 mL h^{-1} (for BiOCl). The distance between the electrodes (needle-tip and the collector) was maintained at about 10 cm. The applied electric voltage between the drum collector and the needle tip was 20 kV and the humidity level inside the electrospinning chamber was maintained at approximately 50%.

BiOCl nanofiber preparation. The BiOCl electrospinning solution is similar to that of the Bi_2O_3, except the precursor $Bi(NO_3)_3 \cdot 5H_2O$ was replaced with $BiCl_3$.

The as-spun free standing nanostructures composed of uniform and continuous nanofibers were collected from the substrate. Later these nanostructures were vacuum dried to completely remove any residual solvents present on the surface. These nanofibers were then calcined at 500 °C for 5 h with a ramp rate of about 5 °C min^{-1} in air, and formed nanosheet-like structures.

Characterization

The surface characterizations of these structures were performed using field emission scanning electron microscopy (FE-SEM; Quanta 200F, FEI, Oregon, U.S.), prior to which the samples were coated with nearly 5 nm of gold (JEOL JFC-1200 fine coater, Japan) for better contrast. Transmission electron microscopy (TEM; JEOL JEM-2010F) at an acceleration voltage of 200 kV was used to characterize morphology. X-ray photoelectron spectroscopy (XPS; Kratos AXIS UltraDLD, Kratos Analytical Ltd., U.K.), with a mono Al Kα X-ray source ($h\nu$ = 1486.71 eV) and operated at 15 kV and 5 mA, was used to identify the oxidation states of ions from the binding energies of photoelectrons. The pressure in the analysis chamber was maintained at 5×10^{-9} torr during each measurement.

Photocatalytic degradation

A suspension of the nanostructured photocatalyst with ARS aqueous solution was prepared in two steps. In the first step 5 mg of catalyst (BiOCl or Bi_2O_3) was dissolved in 45 mL of deionized (DI) water. In the second step 0.5 mg of ARS dye powder was dissolved in 5 mL of DI water. Then both the solutions were mixed and sonicated for about 30 min to obtain a good dispersion of solution. The initial concentration (C_0) of the dye was noted before being exposed to the UV radiation. Later the dispersed solution was placed in such a way that it was completely surrounded by the light source (<390 nm). After every 10 min of irradiation, about 5 mL of the mixture was removed and centrifuged (Allegra 64R centrifuge, Beckman coulter) to remove the residues, and the UV spectra were measured for the supernatants (containing ARS).

Results and discussion

Surface characterization

As-spun nanofibers were characterized by FE-SEM and are shown in Fig. 1. It can be clearly seen that the nanofibers are randomly distributed throughout the area covered. The fibers spun from PAN/$Bi(NO_3)_3 \cdot 5H_2O$ have smooth and uniform textured surfaces because of the amorphous nature of the PAN/$Bi(NO_3)_3 \cdot 5H_2O$ (Fig. 1a–d). In contrast, the fibers from PAN/$BiCl_3$ exhibit a rough textured morphology with continuous structures as shown in Fig. 1e–h. The average fiber diameters evaluated from the SEM images are 1 to 2 μm.

Upon calcination, the smoothly textured fiber morphology of Bi_2O_3 became converted to a porous morphology consisting of nanorods as shown in Fig. 2a–d. For all concentrations of $Bi(NO_3)_3 \cdot 5H_2O$, the nanostructures are porous due to shrinkage resulting from the decomposition of PAN at high temperatures. As seen in these SEM images, the fiber morphology is lost and the nanostructures become more like nanorod/nanotube-conjoined structures, which is due to the complete decomposition of the PAN polymer. The observed diameter of the nanostructures ranged from 40 nm to a few hundred nanometers. Formation of these elongated nanorods may be attributed to an anisotropic growth rate of the bismuth compound nanofibers. Huang, *et al.*[29] reported that there is an increase in electrical potential for nanofibers with rougher surfaces. It has also been reported that the longer polymerization time for the nanofibers also led to the formation of polymer clusters and particles on the surface of nanofibers, making the surface rougher.[30]

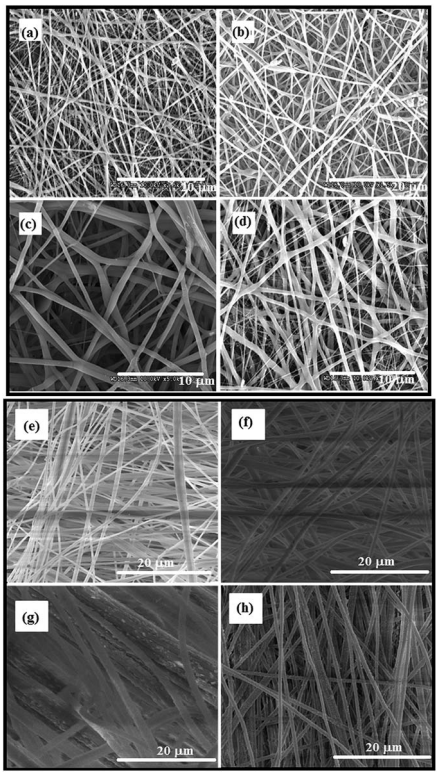

Fig. 1 SEM images of as-spun nanofibers of Bi_2O_3 (a, b, c, d are 1, 2, 3 and 4% respectively) and BiOCl (e, f, g, and h are 1, 2, 3 and 4% respectively).

Fig. 2e–h, shows the BiOCl nanostructures after calcination at about 500 °C for 5 hours. At the low BiOCl precursor concentrations (1, 2 wt%), the resulting structures as shown in Fig. 2e and f are not well defined and they overlap each other. But at high concentrations (3 and 4 wt%), as seen in Fig. 2g and h, the structures display nanosheets with anisotropic dimensions, and a unique nano-stack morphology with an average thickness and length of 700–800 nm and ~2 μm respectively. These FE-SEM images show that the nanosheets appear to be located next to each other and that they are uniformly distributed within the scanning range. The lengths and widths of the nanosheets range up to about ~12–15 μm. Fig. 3 shows the TEM images of the BiOCl and Bi_2O_3 nanostructures. Fig. 3a reveals that the Bi_2O_3 nanostructures are well-defined, relatively long particles with an average dimension of ~200 nm. Bi_2O_3 is more vulnerable to electron-beam irradiation than is BiOCl, and hence Bi_2O_3 is very difficult to observe in high-resolution TEM images. This suggests that BiOCl would be the preferred compound for photocatalysis.

The structures of BiOCl and Bi_2O_3 were characterized by using powder X-ray diffraction (XRD) with CuKα (1.5418 Å) radiation as shown in Fig. 4. The XRD patterns are shown only for the highest level of doping (4 wt%) and after calcination at 500 °C. All of the XRD peaks have been identified and indexed. BiOCl belongs to the tetragonal space group *P*4/*nmm* according to the literature,[31–33] whereas Bi_2O_3 exhibits the β-Bi_2O_3 phase (space group: *P*421*c*).[34–36] The lattice parameters and crystallite sizes were calculated according to the Debye–Scherrer formula ($D = k\lambda/\beta \cos\theta$),[37] where λ is the wavelength of the X-ray (1.5418 Å for CuKα), θ is the angle of diffraction, β is the full width at half maximum (FWHM) and k is the shape factor (=0.94 for spherical crystals with cubic symmetry). The calculated cell parameters are shown in Table 1. Since the volume of the Bi_2O_3 is larger than that of BiOCl, the photodecomposition of Bi_2O_3 may take a longer time. The crystal structure of BiOCl is composed of layers of Cl^-, Bi^{+3} and O^{-2} ions and the ionic distances are d_{Bi-Cl} (3.06 Å) and d_{Bi-O} (2.32 Å).

XPS survey spectra of BiOCl and Bi_2O_3 are shown in Fig. 5. As demonstrated in Fig. 5, Bi, Cl, O and C are detected in the composite nanosheets by scanning high-resolution XPS spectra.

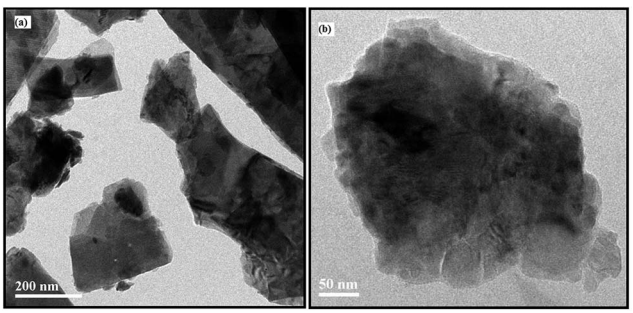

Fig. 3 TEM images of nanosheets of (a) Bi_2O_3 and (b) BiOCl.

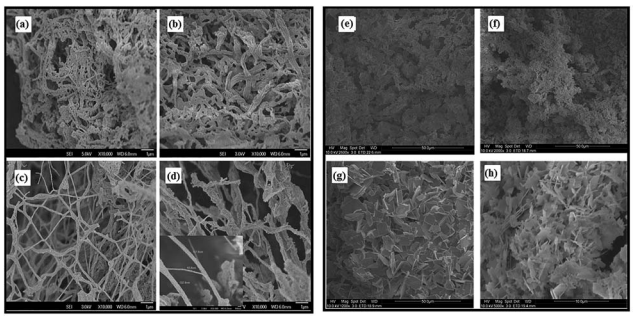

Fig. 2 SEM images after calcination of Bi_2O_3 (a, b, c, d are 1, 2, 3 and 4% respectively) and BiOCl (e, f, g, and h are 1, 2, 3 and 4% respectively).

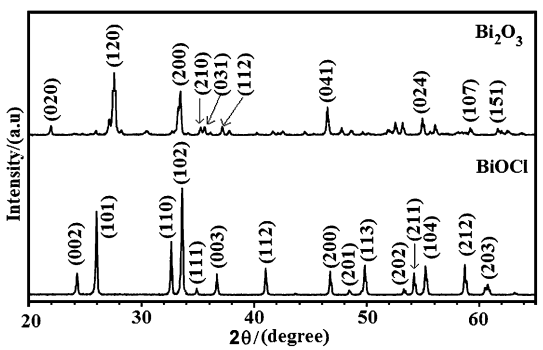

Fig. 4 Typical powder X-ray diffraction patterns of Bi_2O_3 and BiOCl after calcination at 500 °C, at highest concentrations (x = 4%).

The individual core levels of the nanostructures and their corresponding binding energies (BE) are presented in Fig. 6. The Bi4f of BiOCl, shown in Fig. 6a, comprises two asymmetric broad peaks, assigned to the $Bi4f_{7/2}$(BE; 159.1 eV) and $Bi4f_{5/2}$(BE; 164.2 eV). These two peaks were deconvoluted and the peaks at 164.8 and 160.0 eV are indexed as Bi^{+3} in BiOCl.[38–41]

The peaks at 164.1 and 159.1 for BiOCl can be indexed to lower Bi ionic states and are due to the oxygen vacancies present in the system.[42] The appearance of the lower BE peaks might be due to the oxygen vacancies induced from the +3 ionic states.[43–46] Essentially these same peaks, at 164.4 and 159.1 eV, and with the same intensity level, are observed for Bi_2O_3 as illustrated in Fig. 6b. The $4f_{7/2}$ and $4f_{5/2}$ orbitals were formed from the bismuth oxide species during the calcination process. However, the energy differences between $4f_{7/2}$ and $4f_{5/2}$ are ~5.1 eV for BiOCl and 5.3 eV for Bi_2O_3, which are approximately the same and which indicates that the main valence state of Bi in both nanostructures is Bi^{+3}.[40,47] The Cl2p spectra for BiOCl is shown in Fig. 6c. There is a broad 2p peak, which can be decomposed to triplet peaks at 198.1 and 199.0 eV, and which are assigned to $Cl2p_{3/2}$ and $Cl2p_{1/2}$, respectively. The ~0.9 eV energy difference between these two peaks is a characteristic feature for Cl^- anions. This result further confirms the presence of chlorine atoms in the BiOCl fibre nanostructures. Another peak at 195.7 eV corresponds to a defect peak. As for the O1s spectrum shown in Fig. 6d, a broad peak is identified and the shape of this peak indicates that there can be more than one chemical state according to the binding energy. This peak is decomposed at the binding energies of 527.6, 529.0, 530.1, and 531.3 eV for both nanostructures.[48,49] The increased binding energies are simply related to the crystal lattice oxygen (O_{Bi-O}), surface hydroxyl groups (O_{OH}), and adsorbed water. The peak at 529.0 eV is assigned to oxygen bound to trivalent Bi ions and the small shoulder at 531.3 eV implies that the surface is partially covered with hydroxide OH groups.[50] The binding energies related to carbon (C1s) for BiOCl and Bi_2O_3 are 284.8 and 284.6 eV respectively, as presented in Fig. SI1 (ESI),† and are due to a surface layer of carbon contamination. The C1s peak of PAN at 286.5 eV is a related carbon species that has not been identified, implying that the organic species has been degraded completely[51] during calcination at 500 °C.

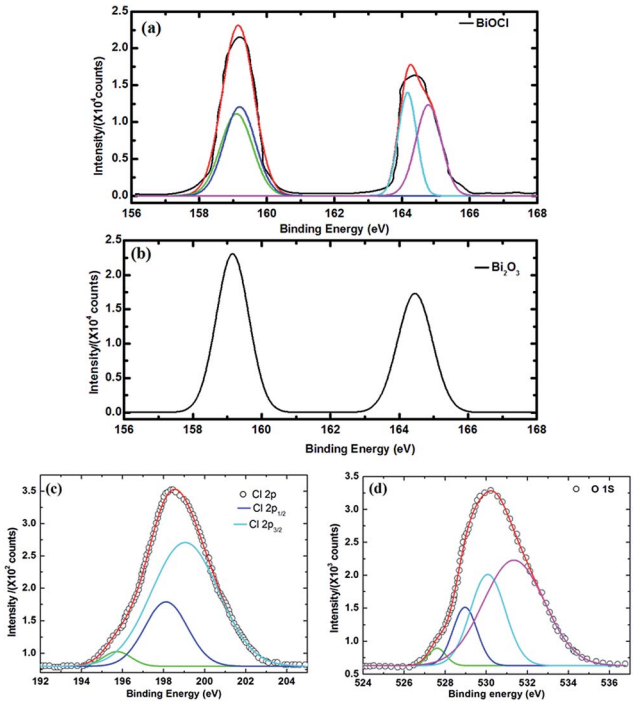

Fig. 6 High-resolution XPS spectra of (a) Bi4f in BiOCl; (b) Bi4f in Bi_2O_3; (c) Cl2p in BiOCl shows three contributions at 195.7, 198.1, and 199.0 eV, related to the defect band, $Cl2p_{3/2}$ and $Cl2p_{1/2}$ respectively; and (d) O1s core levels show bands at 527.6, 529.0, 530.1, and 531.3 eV.

Table 1 Calculated lattice parameter and crystallite sizes from XRD data. *a*, and *c* are the unit cell parameters

	Lattice parameters		Cell volume (Å^3)	Crystallite size (Å)
	a (Å)	*c* (Å)		
BiOCl	3.8817	7.3682	111.02	2.96
Bi_2O_3	7.7408	5.6338	337.57	2.95

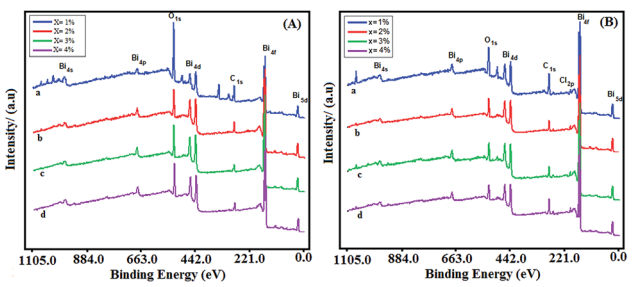

Fig. 5 XPS survey spectra of (A) Bi_2O_3 Bi_2O_3 (a, b, c, d are 1, 2, 3 and 4% respectively) and (B) BiOCl (e, f, g, and h are 1, 2, 3 and 4% respectively).

Photocatalysis and photodegradation

To study the photodegradation, UV-irradiated ARS dye solutions with and without catalyst need to be investigated. And, in the present studies, the PCA properties of ARS dye with and without photocatalysts have been determined under UV-light irradiation. The corresponding photocatalysis studies after incorporation of BiOCl and Bi_2O_3 nanostructures were analyzed and illustrated in Fig. SI2 and SI3.† The ARS solution was red with and without the addition of catalyst nanostructures. But while decolourization was not observed without catalyst, a change in colour was observed after adding the catalysts. These observations indicate that there is no significant degradation and decolorization of ARS dye in the absence of the photocatalyst. Upon UV irradiation of the ARS solution containing the catalysts, degradation was caused and observed as decolourisation of the reaction solution from red to pale pink or white. BiOCl performed better than did Bi_2O_3. The superior degradation performance of BiOCl was due to the difference in sizes of the

catalysts as this also influences the adsorption of the dye molecules.

The related degradation curves with varying concentrations of the precursor are shown in Fig. 7, and the rates of degradation calculated from these curves are tabulated in Table 2. Bi_2O_3 at a concentration of 2% caused significantly faster PCA than it did at any of the other three concentrations. The faster PCA may be because of the morphology change: nanofibers were converted to highly porous nanorods at that particular concentration, as seen in Fig. 2b. BiOCl shows a PCA enhancement at a concentration of 3%, where the nanosheet-like structures were formed (see Fig. 2g).

The photoreaction curves for Bi_2O_3 were also plotted and are shown in Fig. 7a, The photodegradation rate (C/C_0) of the dye with different concentrations (1, 2, 3, and 4%) of precursor were observed under UV light irradiation within the marked time spans, where 'C_0' is the initial concentration of the dye at time T = '0', and 'C' is the final concentration at time T = 't'. From the observations of the absorption spectrum (SI2†), the degradation is over 75%, indicating excellent photocatalytic efficiency (η%). The efficiency was high, at 76.53%, with a Bi_2O_3 precursor concentration of 2%, where the morphology is quite different than for the other concentrations. The other concentrations also showed relatively good photocatalytic efficiencies within 130 min (73.14, 73.72, and 75.38% for 1, 3, and 4% respectively). As the concentration of the catalyst was initially increased, the photocatalytic rate efficiency reached an optimum, and then started to come down with additional increases in concentration. Fig. 7b, shows the photocatalytic degradation of BiOCl and an aqueous solution of ARS under UV-light illumination. It can be noted that the absorption band of the dye degraded rapidly at the precursor concentration level of 3% and complete degradation happened in 70 min. For the other concentrations (1, 2 and 4%), the degradation process went on for 80 min. The rapid photodegradation rate as shown in Fig. 7b is probably because of the ordered morphology of the nanosheets, whereas at the first two concentrations (1 and 2%), no clear morphology could be seen in the SEM images (Fig. 2e and f). The highest efficiency was found at the concentration x = 3%, the value being 99.34%. The other concentrations (1, 2 and 4%) also showed relatively good photocatalytic efficiencies, being a little lower at 88.54, 96.94, and 92.34% for x = 1, 2, and 4% respectively.

The kinetics plots of Bi_2O_3, and BiOCl are presented in Fig. 8 and 9. Both of the nanostructures follow pseudo first-order kinetics. From the kinetic plots, the rate constants were determined by linear polynomial fitting of the $\ln(C/C_0)$ curve and the rate constant 'k' values were evaluated from the equation, $k = 2.303 \times \log(C/C_0)$ and presented in Table 2. The rate constant at 2% and 3% dopings of Bi_2O_3 and BiOCl shows the best degradation performance, since at those concentrations the morphology of the catalysts was quite different.

From pseudo first-order kinetic constants, the half-life time ($t_{1/2}$) can be calculated using the expression $t_{1/2} = 0.693/k$. According to the half-life expression, the half-life of the dye

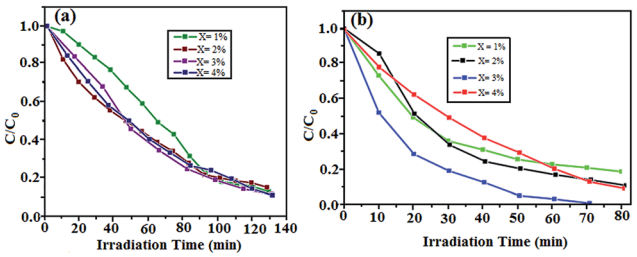

Fig. 7 Photocatalytic ARS dye degradation of (a) Bi_2O_3 and (b) BiOCl under UV-irradiation.

Table 2 Kinetic constants and their calculated half-life time in minutes[a]

	x = 1%		x = 2%		x = 3%		x = 4%	
	k	$t_{1/2}$	k	$t_{1/2}$	k	$t_{1/2}$	k	$t_{1/2}$
Bi_2O_3	0.124	5.584	0.165	4.141	0.141	4.933	0.136	5.106
BiOCl	0.133	5.207	0.152	3.530	0.196	4.568	0.138	5.036

[a] x represents the concentrations, k is the kinetic constant and $t_{1/2}$ is the half-life of the catalyst.

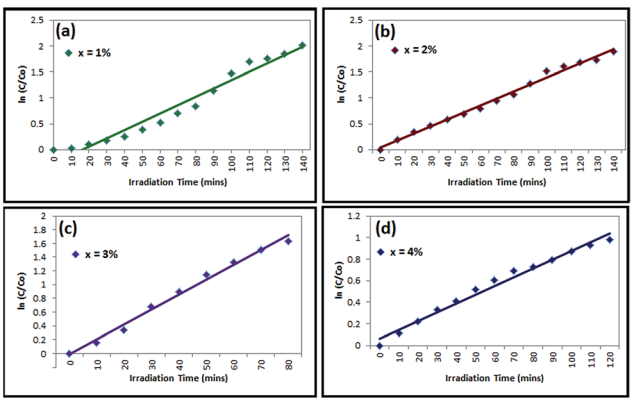

Fig. 8 Kinetic plots and rate constant evaluation of Bi_2O_3 photocatalyst at (a) x = 1%, (b) x = 2%, (c) x = 3% and (d) x = 4% (w/v).

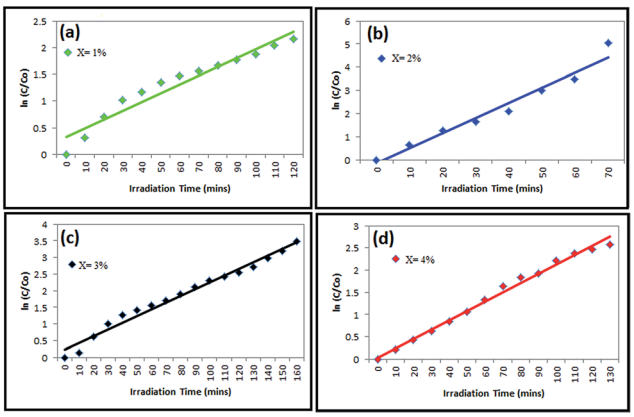

Fig. 9 Kinetic plots and rate constant evaluation of BiOCl photocatalyst at (a) x = 1%, (b) x = 2%, (c) x = 3% and (d) x = 4% (w/v).

degradation has been evaluated and tabulated in Table 2. It also suggests that the BiOCl is an excellent photocatalyst for the industrial dye degradation, and is superior to Bi_2O_3.

Dye degradation mechanism

The BiOCl nanosheet-like structures showed significant PCA enhancement in the decomposition of ARS dye. In general, the PCA of the catalyst is dependent on several factors such as surface properties, crystallinity, morphology, optical properties, and diameter.[52] From XRD analysis, crystal structures were not changed much, which had minimal effect in PCA performance. It is worth noting that the morphology of BiOCl changed into nanosheet-like structures that might adsorb more dye molecules at the surface. The PCA reaction might be preceded by two steps:[32,53] adsorption, and degradation after the adsorption. Thus, the stronger the adsorption capability, the better would be the subsequent photodegradation.

The possible mechanism for ARS dye degradation in the presence of BiOCl catalyst has been proposed and is presented in Fig. 10. The conduction band (CB) and valance band (VB) potentials of BiOCl are −1.10 and −2.20 eV respectively,[32] and the band gap is hence 3.3 eV.[1,54] The ARS dye is adsorbed on the surface of the catalyst (BiOCl). Photogenerated electrons transfer from VB to CB, leaving holes behind VB atop of the ARS dye. Then the excited electrons react with the oxygen to form O_2^-. Then these oxygen radicals and holes can effectively oxidize the ARS dye. Thus, two mechanisms may be involved in the degradation.[25]

$$B_{(catalyst)} + h\nu \rightarrow h^+ + e^- \quad (1)$$

$$e^- + O_2 \rightarrow {}^{\bullet}O_2^- \text{ (radical)} \quad (2)$$

$$h^+ + OH^- \rightarrow {}^{\bullet}OH \text{ (radical)} \quad (3)$$

$$ARS^*_{(dye.ads)} + B_{(catalyst)} \rightarrow B_{(catalyst)}(e^-) + ARS_{(dye.ads)}{}^+ \quad (4)$$

$$B_{(catalyst)}(e^-) + O_2 \rightarrow B_{(catalyst)} + {}^{\bullet}O_2^- \text{ (radical)} \quad (5)$$

$$B_{(catalyst)} + {}^{\bullet}O_2^- + 2H^+ \rightarrow B_{(catalyst)} + {}^{\bullet}OH \text{ (radical)} \quad (6)$$

$$ARS_{(dye.ads)} + {}^{\bullet}O_2^- \rightarrow \text{Products} \quad (7)$$

In eqn (1)–(7), B stands for BiOCl, and dye.ads stands for adsorbed dye. These equations provide mechanisms for photoadsorption and consequent dye degradation.

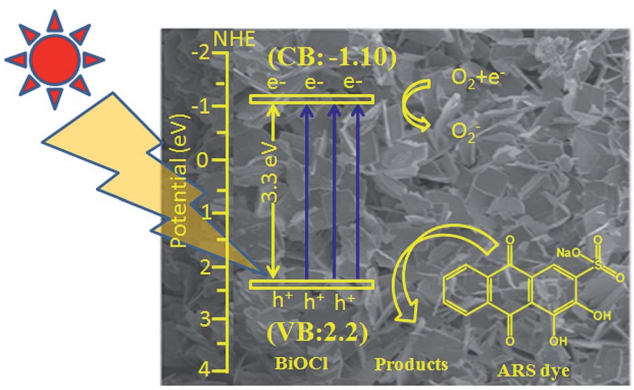

Fig. 10 Schematic representation of oxidation and reduction in BiOCl.

Conclusions

Electrospun sheet/rod-shaped nanostructures have been produced. By changing the precursor concentration, changes in the morphology of Bi_2O_3 and BiOCl nanostructures have been observed from SEM, and TEM confirmed their morphologies. During calcination, the dynamics of the polymers vary and the collective interaction between the precursors causes anisotropic crystal formation. XRD reveals the tetragonal and β-phases of BiOCl and Bi_2O_3 respectively. From XPS, it is confirmed that Bi in these structures exists in the Bi^{+3} ionic state, and in lower ionic states as well. The converted nanostructures are employed for the photodegradation of ARS dye. As the size of the crystallite increases (determined from XRD), the photodecomposition ability substantially decreases. Therefore, the enhancement of PCA is due to the change in morphology, such as that into nanosheet-like structures. Possible degradation mechanisms for the dye have been proposed and discussed. We anticipate that our investigations may help further understanding of various nanostructured materials and accelerate their potential applications.

Acknowledgements

All the authors thank M3TC (EDB) R-261-501-018-414, Singapore for providing financial assistance. V J Babu thanks The Scientific & Technological Research Council of Turkey (TUBITAK) (TUBITAK-BIDEB 2221, Fellowships for visiting scientists and scientists on sabbatical leave) for providing fellowship support.

Notes and references

1 H. Cheng, B. Huang and Y. Dai, *Nanoscale*, 2014, **6**, 2009–2026.
2 K.-L. Zhang, C.-M. Liu, F.-Q. Huang, C. Zheng and W.-D. Wang, *Appl. Catal., B*, 2006, **68**, 125.
3 Y. Bessekhouad, D. Robert and J.-V. Weber, *Catal. Today*, 2005, **101**, 315–321.
4 W. Xiaohong, Q. Wei and H. Weidong, *J. Mol. Catal. A: Chem.*, 2007, **261**, 167–171.
5 L. Zhang, W. Wang, J. Yang, Z. Chen, W. Zhang, L. Zhou and S. Liu, *Appl. Catal., A*, 2006, **308**, 105–110.
6 H. Peng, C. K. Chan, S. Meister, X. F. Zhang and Y. Cui, *Chem. Mater.*, 2009, **21**, 247–252.
7 G. G. Briand and N. Burford, *Chem. Rev.*, 1999, **99**, 2601–2658.
8 S. K. Poznyak and A. I. Kulak, *Electrochim. Acta*, 1990, **35**, 1941–1947.
9 D. O. Charkin, P. S. Berdonosov, V. A. Dolgikh and P. Lightfoot, *J. Solid State Chem.*, 2003, **175**, 316–321.

10 N. Kijima, K. Matano, M. Saito, T. Oikawa, T. Konishi, H. Yasuda, T. Sato and Y. Yoshimura, *Appl. Catal., A*, 2001, **206**, 237–244.
11 X. Zhang, Z. Ai, F. Jia and L. Zhang, *J. Phys. Chem. C*, 2008, **112**, 747–753.
12 W. Xiaohong, Q. Wei and H. Weidong, *J. Mol. Catal. A: Chem.*, 2007, **261**, 167–171.
13 X. Lin, T. Huang, F. Huang, W. Wang and J. Shi, *J. Phys. Chem. B*, 2006, **110**, 24629–24634.
14 L. Zhang, J. Li, Z. Chen, Y. Tang and Y. Yu, *Appl. Catal., A*, 2006, **299**, 292–297.
15 J. C. Yu, J. Yu, W. Ho and L. Zhang, *Chem. Commun.*, 2001, 1942–1943.
16 T. Park, S. A. Haque, R. J. Potter, A. B. Holmes and J. R. Durrant, *Chem. Commun.*, 2003, 2878–2879.
17 Z. Liu, D. D. Sun, P. Guo and J. O. Leckie, *Nano Lett.*, 2007, **7**, 1081–1085.
18 Y. Wu, H. Yan and P. Yang, *Top. Catal.*, 2002, **19**, 197–202.
19 J. Zhu and M. Zäch, *Curr. Opin. Colloid Interface Sci.*, 2009, **14**, 260–269.
20 V. J. Babu, A. S. Nair, Z. Peining and S. Ramakrishna, *Mater. Lett.*, 2011, **65**, 3064–3068.
21 X. Hu, G. Li and J. C. Yu, *Langmuir*, 2010, **26**, 3031–3039.
22 P. Balaya, *Energy Environ. Sci.*, 2008, **1**, 645–654.
23 V. J. Babu, D. V. B. Murthy, V. Subramanian, V. R. K. Murthy, T. S. Natarajan and S. Ramakrishna, *J. Appl. Phys.*, 2011, **109**, 074306.
24 M. R. Hoffmann, S. T. Martin, W. Choi and D. W. Bahnemann, *Chem. Rev*, 1995, **95**, 69.
25 J. B. Veluru, S. R. S. Bhavatharini and S. Ramakrishna, *RSC Adv.*, 2014, **4**, 19251–19256.
26 J. B. Veluru, K. K. Manippady, M. Rajendiren, K. M. Mya, P. R. Rayavarapu, S. N. Appukuttan and R. Seeram, *Int. J. Hydrogen Energy*, 2013, **38**, 4324–4333.
27 V. J. Babu, M. K. Kumar, A. S. Nair, T. L. Kheng, S. I. Allakhverdiev and S. Ramakrishna, *Int. J. Hydrogen Energy*, 2012, **37**, 8897–8904.
28 C. Wang, C. Shao, L. Wang, L. Zhang, X. Li and Y. Liu, *J. Colloid. Interface Sci.*, 2009, **333**, 242–248.
29 Z. M. Huang, Y. Z. Zhang, M. Kotaki and S. Ramakrishna, *Compos. Sci. Technol.*, 2003, **63**, 2223–2253.
30 Z. Wang, Z.-Z. Zhu, J. Shi and H.-L. Li, *Appl. Surf. Sci.*, 2007, **253**, 8811–8817.
31 L. Q. Ye, L. Zan, L. H. Tian, T. Y. Peng and J. J. Zhang, *Chem. Commun.*, 2011, **47**, 695–697.
32 T. Xie, L. Xu, C. Liu, J. Yang and A. M. Wang, *Dalton Trans.*, 2014, **43**, 2211–2220.
33 H. Liu, W. Yang, Y. Ma and J. Yao, *Appl. Catal., A*, 2006, **299**, 218–223.
34 B. Gao, Y. J. Kim, A. K. Chakraborty and W. I. Lee, *Appl. Catal., B*, 2008, **83**, 202.
35 M. Gotić, S. Popović and S. Musić, *Mater. Lett.*, 2007, **61**, 709–714.
36 H. Cheng, B. Huang, J. Lu, Z. Wang, B. Xu, X. Qin, X. Zhang and Y. Dai, *Phys. Chem. Chem. Phys.*, 2010, **12**, 15468–15475.
37 J. I. Langford and A. J. C. Wilson, *J. Appl. Crystallogr.*, 1978, **11**, 102–113.
38 H. An, Y. Du, T. Wang, C. Wang, W. Hao and J. Zhang, *Rare Met.*, 2008, **27**, 243–250.
39 Y. Wu, M. Xing, J. Zhang and F. Chen, *Appl. Catal., B*, 2010, **97**, 182–189.
40 W. E. Morgan, W. J. Stec and J. R. V. Wazer, *Inorg. Chem.*, 1973, **12**, 953–955.
41 J.-M. Song, C.-J. Mao, H.-L. Niu, Y.-H. Shen and S.-Y. Zhang, *CrystEngComm*, 2010, **12**, 3875–3881.
42 L. Ye, K. Deng, F. Xu, L. Tian, T. Peng and L. Zan, *Phys. Chem. Chem. Phys.*, 2012, **14**, 82–85.
43 X. Chen, L. Liu, P. Y. Yu and S. S. Mao, *Science*, 2011, **331**, 746–750.
44 M. Batzill, E. H. Morales and U. Diebold, *Chem. Phys.*, 2007, **339**, 36–43.
45 C. Rath, P. Mohanty, A. C. Pandey and N. C. Mishra, *J. Phys. D: Appl. Phys.*, 2009, **42**, 205101.
46 G. Liu, H. G. Yang, X. Wang, L. Cheng, H. Lu, L. Wang, G. Q. M. Lu and H.-M. Cheng, *J. Phys. Chem. C*, 2009, **113**, 21784–21788.
47 V. S. Dharmadhikari, S. R. Sainkar, S. Badrinarayan and A. Goswami, *J. Electron Spectrosc. Relat. Phenom.*, 1982, **25**, 181–189.
48 http://www.lasurface.com/database/elementxps.php.
49 http://srdata.nist.gov/xps/selEnergyType.aspx.
50 C. Wang, C. Shao, X. Zhang and Y. Liu, *Inorg. Chem.*, 2009, **48**, 7261–7268.
51 C. Wang, C. Shao, Y. Liu and L. Zhang, *Scr. Mater.*, 2008, **59**, 332–335.
52 I.-S. Cho, S. Lee, J. H. Noh, G. K. Choi, H. S. Jung, D. W. Kim and K. S. Hong, *J. Phys. Chem. C*, 2008, **112**, 18393–18398.
53 J. Di, J. Xia, S. Yin, H. Xu, L. Xu, Y. Xu, M. He and A. H. Li, *RSC Adv.*, 2014, **4**, 14281–14290.
54 L.-P. Zhu, G.-H. Liao, N.-C. Bing, L.-L. Wang, Y. Yang and H.-Y. Xie, *CrystEngComm*, 2010, **12**, 3791–3796.